Neural Networks 47 (2013) 51–63

Contents lists available at ScienceDirect

Neural Networks

journal homepage: www.elsevier.com/locate/neunet

2013 Special Issue

Solution to the inverse problem of estimating gap-junctional and inhibitory conductance in inferior olive neurons from spike trains by network model simulation

Miho Onizuka [a,b,1], Huu Hoang [b,c,1], Mitsuo Kawato [d,a,1], Isao T. Tokuda [c], Nicolas Schweighofer [e], Yuichi Katori [f,g], Kazuyuki Aihara [g], Eric J. Lang [h], Keisuke Toyama [b,*]

[a] Graduate School of Information Science, Nara Advanced Institute of Science and Technology, 8916-5 Takayama, Ikoma, Nara 630-0192, Japan
[b] ATR Brain Information Communication Research Laboratories, 2-2-2 Hikaridai, Seika-cho, Soraku-gun, Kyoto 619-0288, Japan
[c] Department of Mechanical Engineering, Ritsumeikan University, 1-1-1 Nojihigashi, Kusatsu-shi, Shiga 525-8577, Japan
[d] ATR Computational Neuroscience Laboratories, 2-2-2 Hikaridai, Seika-cho, Soraku-gun, Kyoto 619-0288, Japan
[e] Biokinesiology and Physical Therapy, University of Southern California, 1540 Alcazar Street, CHP 155, Los Angeles, CA 90089-9006, USA
[f] FIRST Aihara Innovative Mathematical Modelling Project, JST, Tokyo, Japan
[g] Institute of Industrial Science, University of Tokyo, 4-6-1 Komaba Meguro-ku, Tokyo 153-8505, Japan
[h] Department of Physiology & Neuroscience, School of Medicine, New York University, New York, NY 10016, USA

ARTICLE INFO

Keywords:
Inferior olive
Cerebellum
Gap junction
PCA
ANOVA

ABSTRACT

The inferior olive (IO) possesses synaptic glomeruli, which contain dendritic spines from neighboring neurons and presynaptic terminals, many of which are inhibitory and GABAergic. Gap junctions between the spines electrically couple neighboring neurons whereas the GABAergic synaptic terminals are thought to act to decrease the effectiveness of this coupling. Thus, the glomeruli are thought to be important for determining the oscillatory and synchronized activity displayed by IO neurons. Indeed, the tendency to display such activity patterns is enhanced or reduced by the local administration of the GABA-A receptor blocker picrotoxin (PIX) or the gap junction blocker carbenoxolone (CBX), respectively. We studied the functional roles of the glomeruli by solving the inverse problem of estimating the inhibitory (g_i) and gap-junctional conductance (g_c) using an IO network model. This model was built upon a prior IO network model, in which the individual neurons consisted of soma and dendritic compartments, by adding a glomerular compartment comprising electrically coupled spines that received inhibitory synapses. The model was used in the forward mode to simulate spike data under PIX and CBX conditions for comparison with experimental data consisting of multi-electrode recordings of complex spikes from arrays of Purkinje cells (complex spikes are generated in a one-to-one manner by IO spikes and thus can substitute for directly measuring IO spike activity). The spatiotemporal firing dynamics of the experimental and simulation spike data were evaluated as feature vectors, including firing rates, local variation, auto-correlogram, cross-correlogram, and minimal distance, and were contracted onto two-dimensional principal component analysis (PCA) space. g_c and g_i were determined as the solution to the inverse problem such that the simulation and experimental spike data were closely matched in the PCA space. The goodness of the match was confirmed by an analysis of variance (ANOVA) of the PCA scores between the experimental and simulation spike data. In the PIX condition, g_i was found to decrease to approximately half its control value. CBX caused an approximately 30% decrease in g_c from control levels. These results support the hypothesis that the glomeruli are control points for determining the spatiotemporal characteristics of olivocerebellar activity and thus may shape its ability to convey signals to the cerebellum that may be used for motor learning or motor control purposes.

* Corresponding author.
E-mail address: toyama@atr.jp (K. Toyama).

[1] These three authors contributed equally to this study.

0893-6080/$ – see front matter © 2013 Elsevier Ltd. All rights reserved.
doi:10.1016/j.neunet.2013.01.006

1. Introduction

The inferior olive (IO) possesses complex synaptic structures called glomeruli. Dendritic spines of neighboring IO neurons project into a glomerulus and are electrically coupled via gap junctions (Llinás, Baker, & Sotelo, 1974; Llinás & Yarom, 1981; Sotelo, Llinás, & Baker, 1974). Contacting these spines are presynaptic terminals, about half of which are GABAergic, and, for most IO regions, arise from cells of the deep cerebellar nuclei (DCN) (De Zeeuw, Holstege, Ruigrok, & Voogd, 1989; Sotelo, Gotow, & Wassef, 1986). Multichannel recording of Purkinje cell complex spikes has elucidated the complicated spatiotemporal dynamics of IO firing, including synchronization, oscillation, and chaotic activity (Lang, 2002; Lang, Sugihara, Welsh, & Llinás, 1999; Llinás & Sasaki, 1989). The glomeruli are thought to be a key structure for determining IO dynamics. Consistent with this idea, complex spike firing dynamics were altered in distinct ways by the local administration of GABA blocker picrotoxin (PIX) or gap-junction blocker carbenoxolone (CBX), respectively (Blenkinsop & Lang, 2006; Lang, 2002; Lang, Sugihara, & Llinás, 1996). In particular, PIX increases complex spike synchrony and CBX reduces it. However, the actions of these drugs are not limited to the glomeruli. For example, GABAergic synapses occur at both intra- and extra-glomerular sites (Sotelo et al., 1986).

To provide evidence that changes specifically within the glomeruli can lead to changes in IO firing dynamics, we used a neural network modeling approach. We started by modifying an earlier model of the IO that consisted of electrically coupled neurons (Schweighofer et al., 2004). In that model, the neurons consisted of only two compartments (soma and dendrite) and the electrical coupling occurred between dendritic compartments of neighboring cells. To our best knowledge, there was no IO model with spines. Thus, in the present model, we add a glomerular compartment to each IO neuron, which consists of a dendritic spine that receives an inhibitory synaptic conductance, and we have the electrical coupling between IO neurons occurring only between these spines. This new model allows us to test how the local interactions between gap-junctional and inhibitory chemical synaptic signals shape IO spiking patterns. Specifically, we use a Bayesian approach to determine the gap-junctional and inhibitory conductance values that best match simulated (SIM) spike trains to experimentally recorded Purkinje cell complex spike activity in control (CON), PIX, and CBX conditions (note that the one-to-one relationship between complex spikes and IO spikes allows using complex spikes as a proxy for IO spikes).

Our results show that the change in firing patterns between experimental (EXP) control and PIX conditions is best simulated by halving the inhibitory conductance in the glomerular compartment, whereas the change in firing patterns from control to CBX were best modeled by a 1/3 reduction in the electrical coupling between spines. These results support the hypothesis that inhibitory synaptic activity and electrical coupling within glomeruli strongly shape the firing properties of the olivocerebellar system.

2. Methods

In order to study the synaptic mechanisms underlying the experimentally observed dynamics of IO activity, we used a Bayesian approach to solve the inverse problem of simulating the firing dynamics from a given conductance parameter set. That is, spike train data sets were generated for step-wise variations of the two model parameters of interest here, the inhibitory synaptic (g_i) and gap-junctional (g_c) conductances. The SIM data set for each variation of g_i and g_c was then compared with the EXP spike data, and the parameters for the simulation data that best fit to the experimental control, PIX, and CBX conditions were selected as the solutions to the inverse problem. Changes in the solutions across the three conditions allowed us to infer how changes in the state of the IO glomeruli relate to the patterns of spiking generated by this system.

To use this approach, two issues needed to be addressed. The first was the problem of how to evaluate the complicated dynamics of the EXP data in order to be able to estimate the goodness of the fit between the SIM and EXP data. This was resolved by using a feature vector (FV)-principal component analysis (PCA) approach in which many FVs (i.e., quantitative measures of the spike activity) were used to capture various aspects of IO activity. Next, PCA was used to reduce the FV data to a two-dimensional PCA space, where the distance (fitting error) between the EXP and SIM data was then estimated.

The second difficulty was that of how to use the FV-PCA approach given that the dynamics of IO neurons vary in time, and from neuron to neuron. One possibility is to compare average FVs based on analysis of the entire EXP and SIM data sets. Instead, we used a segment-wise fitting approach that fractionated the EXP and SIM data into spatiotemporal segments (short time segments and small neuronal subgroups), and searched for the SIM data of the best fit (i.e., the one with the minimum error from the EXP one), segment by segment. The segment-wise fitting resolved the inverse problem in a probabilistic fashion as en ensemble of the g_i and g_c estimates (one for each segment). The reliability of the segment-wise Bayesian estimates was examined by analysis of variance (ANOVA) to test the statistical significance of the difference between the mean PCA scores of the SIM and EXP data segments compared to their variances. It is worth noting that the segment-wise fitting far outperformed the conventional mean-based fitting with respect to error rate, where the former being two orders of magnitude smaller than the latter.

Our study to estimate the synaptic conductance of the IO circuitry from neuronal firing using IO network simulation may be regarded as a Bayesian solution to the inverse problem in the following sense. According to Bayes' rule, the posterior probability of the synaptic conductance is given as the product of the likelihood and the prior probability of the synaptic conductance. To obtain a value for the likelihood, the network simulation played the role of the forward model to predict firing dynamics from a given set of synaptic conductances. The match probability between the SIM and EXP data in our analysis then corresponds to the likelihood of a specific EXP data given a specific parameter set. Strictly, the likelihood was approximated by a Gibbs distribution with a low-temperature limit, while the energy term is the squared error between the EXP and SIM firing patterns. Global search assumed the prior probability to be a non-informative uniform distribution, and a "juggling search" that will be introduced later utilized the posterior probability determined by the global search as the prior probability.

The inverse problem to estimate g_c and g_i from IO firing dynamics was resolved in four steps. First, SIM spike data were generated with step-wise variations of g_i and g_c by an IO network model. Second, the complicated firing of the EXP and SIM spike data that vary in space (from neuron to neuron) and time were fractionated into spatiotemporal segments (short spike segments for small groups of neurons) and evaluated in a segment-wise fashion using firing feature vectors (FVs), and the FVs of the spike data segments were contracted onto two-dimensional PCA space. Thus the firing dynamics of the EXP and SIM spike data were mapped onto the PCA space for each spatiotemporal data segment. Third, the g_c and g_i for the SIM spike segments that showed the closest match in the PCA space (i.e., the minimum PCA errors defined as Euclidean distance) to the EXP ones were determined as the solutions to the inverse problem. Fourth, there was an ill-posed problem that the firing dynamics mainly depend on the

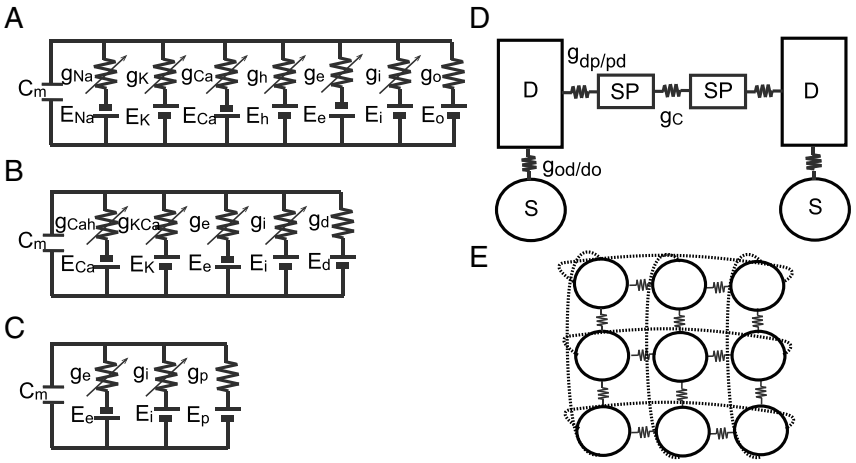

Fig. 1. Schematic diagram illustrating IO neuronal network. A–C: Equivalent circuit models of the membrane per unit area that contains ionic channel conductance, excitatory g_e, and inhibitory g_i synaptic conductance as well as inter-compartmental conductances g_{do}, g_{od}, g_{pd}, g_{dp} and g_c for the soma, dendrite, and spine compartments. D and E: Compartment and network model representing interneuronal connectivity. Dotted lines represent the connectivity that shows the periodic boundary conditions: a torus-like structure. The somatic compartment contains g_{Na}, g_K, g_{Cal}, g_h, and g_o, which are the ionic channel conductances for an inward sodium current, a delayed rectifier outward potassium current, a low-threshold calcium current, an anomalous inward rectifier current, and the leakage current. The dendritic compartment includes ionic channel conductances for high-threshold calcium current g_{Cah}, for calcium-activated potassium current g_{Kca}, and for leakage current g_d. The model structure and parameters essentially follow those of Schweighofer et al. (2004). A Poisson spike generator firing at a mean rate of 10 spikes/s was assumed for each synaptic input, including g_e and g_i. Each cell received 260 excitatory and inhibitory Poisson synaptic inputs (soma: 10, dendrite: 80, spine: 10 multiplied by 2).

ratio of g_c to g_i rather than individuals (Katori, Lang, Onizuka, Kawato, & Aihara, 2010; Onizuka, 2009). This issue was resolved by a "juggling algorithm" in which the match between the SIM and EXP spike segments was searched under the constraint that g_c and g_i remain unaffected by PIX and CBX administration, respectively. In other words, g_c and g_i should agree with each other between CON and PIX conditions and between CON and CBX conditions, respectively.

2.1. IO neuron model

An IO neuronal model was used as the forward model to simulate the firing dynamics of the system. The neurons of the present model were based on those in the model of Schweighofer et al. (2004). In this earlier model, each neuron was composed of only two compartments: soma and dendrite. The connection between these compartments was modeled by the crosstalk conductances from/to the soma and to/from the dendrite (g_{od}, g_{do}). In order to investigate how glomerular characteristics affect IO activity, each neuron in the present model additionally contains four spine compartments connected to the dendritic compartment. As detailed below, the spine compartments contain both gap-junctional and synaptic conductances in order to simulate the physiological interactions that occur within the glomeruli.

The network model consisted of 3×3 array of IO neurons, each of which was mutually connected to its four neighboring neurons by a gap junction from one of its spines to one of its neighbor's (Fig. 1(E)). Each spine compartment was connected to the dendritic compartment by a crosstalk conductance from/to dendrite and to/from spine (g_{dp}, g_{pd}), and mutually connected to the neighboring spine compartments through the gap-junctional conductance (g_c). Throughout this paper, we will use suffixes o, d, and p to denote the somatic, dendritic, and spine compartments. Note that each connection between two compartments is characterized by two direction-specific conductances because conductance was defined per membrane surface area and thus is effectively different according to the direction of current flow (see below).

The major experimentally described conductances of IO neurons are implemented in the model as they were in the earlier cell model (Schweighofer et al., 2004). The somatic compartment contains ionic channel conductances for the inward sodium current (g_{Na}), the delayed rectifier outward potassium current (g_K), the low-threshold calcium current (g_{Cal}), the anomalous inward rectifier current (g_h), and the leakage current (g_o) (Fig. 1(A)). The dendritic compartment includes ionic channel conductances for the high-threshold calcium current (g_{Cah}), the calcium-activated potassium current (g_{Kca}), and the leakage current (g_d) (Fig. 1(B)). The spine compartment includes a conductance for a leakage current (g_p) (Fig. 1(C)). All three classes of compartment receive excitatory (g_e) and inhibitory (g_i) synaptic conductances driven by Poisson noise generators. All of the ionic, crosstalk, and synaptic conductances are defined for a unit surface area of the soma, dendrite, or spine membrane.

The electrophysiological properties of the IO model also depended on the crosstalk conductances between the soma and dendrite compartments (g_{od}, g_{do}) and between the dendrite and spine compartments (g_{dp}, g_{pd}) (Fig. 1(D)). They are defined per membrane surface area and therefore depend on neuron morphology: the ratio of the somatic area to the total surface area (p), and the ratio of the area of the four spines to the total surface area (q) (see Eqs. (A.9), (A.13), (A.14) and (A.17) in the Appendix).

2.2. Synaptic inputs

The spine compartment is the major new feature of the present version of our model, which allowed us to address the effects of inhibitory synaptic inputs to the glomeruli where the IO neurons are connected to each other with g_c (see Eq. (A.15) in the Appendix for the junctional current). All of the soma, dendrite, and spine compartments receive 10, 80, and 10 excitatory and inhibitory synapses driven by Poisson spike generators (Schweighofer et al., 2004). The numbers of synapses are roughly proportional to the surface areas of the three compartments.

2.3. Network structure

We simulated the dynamics of a network of electrically coupled IO neurons whose coupling is antagonized by shunting inhibition. Model IO neurons had tiny variations from each other (Schweighofer et al., 2004); that is, the maximal conductance g_{Cal}

value of the low-threshold calcium current for each neuron was randomly drawn from a uniform distribution, with the maximum deviation set at ±5% of the mean. The network structure is a toroidally linked 3 × 3 grid of cells, where the cells are connected to their four neighbors at the spine depending on their positions in the grid (Fig. 1(E)). The network structure adopted is for allowing spatial inhomogeneity into the model and for mathematical simplicity.

2.4. Computer simulation

We computed the electrical activity in each compartment of the model with step-wise variations of the gap-junctional conductance (g_c) and the inhibitory conductance (g_i). The other model parameters including the crosstalk conductances (g_{od}, g_{do}, g_{dp}, g_{pd}, and g_c in Eqs. (A.9), (A.13)–(A.15) and (A.17)) were fixed to the values essentially the same as those used by Schweighofer et al. (2004); Schweighofer, Doya, and Kawato (1999), except for the new parameters (g_{dp}, g_{pd}, and q), which are related to the spine compartment and were fixed at the values shown in Table A.1 in the Appendix. The electrical activity in each compartment of the model was simulated with interactions through a system of ordinary differential equations (Eqs. (A.1)–(A.3)) that determines the changes of the membrane potential within the somatic, dendritic, and four spine compartments. Each ordinary differential equation contains many different ionic, crosstalk, and gap-junctional currents, and excitatory and inhibitory synaptic inputs (from Eqs. (A.4)–(A.18)).

We simulated the membrane potential time courses of the nine cells with step-wise changes of the two model parameters, i.e., inhibitory synaptic conductance g_i, and coupling conductance g_c (0.025 step, with range 0–2.0 mS/cm^2) and generated 6561 (=81× 81) sets of 500 s long SIM spike trains. Within these spike trains the time of each spike was defined as the time when the change in the somatic membrane potential exceeded 40 V/s. The numerical integration of the system of ordinary differential equations (A.1)–(A.3) was executed by the CVODE package (part of the SUNDIALS package) with 0.5 ms time steps. For numerically stiff problems like the present IO network model, CVODE includes backward differentiation formulas.

2.5. Spike train analysis

The SIM and EXP spike trains were fractionated into segments (see Fig. 3(A) and (B)), and the firing dynamics were evaluated for each segment using three temporal and two spatial classes of FV. Throughout this paper we use suffixes i, j for the number of neurons, k for time step, and l, m for the number of spikes. The three temporal classes of FV used to characterize the temporal firing properties of the individual neurons were as follows.

(i) The mean firing rate of the entire segment (*FR*), calculated by dividing the number of spikes in a segment by the duration of the segment.

(ii) The auto-correlogram for three delays (*ACG* 1, 2, 3, corresponding to delays of 50–100, 100–150, 150–200 ms), which was calculated as follows:

$$ACG_{x,i}(\tau) = \sum_{k=1}^{K} x_i(t_k)x_i(t_k - \tau), \tag{1}$$

where $x_i\ (t_k)$ represents the occurrence of spikes at the kth time step in the ith neuron; $x_i\ (t_k) = 1$ if a spike is generated in time step t_k, otherwise $x_i\ (t_k) = 0$; and τ is the time delay.

(iii) Local variation (*LV*) (Shinomoto, Miura, & Koyama, 2005), which was calculated by

$$LV = \frac{1}{R-1}\sum_{r=1}^{R}\frac{3(T_r - T_{r+1})^2}{(T_r + T_{r+1})^2}, \tag{2}$$

where T_r ($r = 1, 2, \ldots, R$) is the rth inter-spike interval. *LV* is 1 for Poisson firing and becomes negative and positive for regular and burst firing, respectively.

The following two spatial classes of the FV were used to characterize the spatial firing properties of neuron pairs.

(iv) Cross-correlograms (*CCG* 1, 2, 3, and 4) for four delays (0–50, 50–100, 100–150, 150–200 ms) were calculated by

$$CCG_{x,i,j}(\tau) = \sum_{k=1}^{K} x_i(t_k)x_j(t_k - \tau). \tag{3}$$

(v) The minimal distance (MD), defined as a normalized distribution of the following s (Hirata & Aihara, 2009; Katori et al., 2010) between the lth spike of neuron i and a spike of neuron j, is defined as follows:

$$s_l^{i,j} = 1 - \exp\left(\frac{-2\min_m |t_l^i - t_m^j|}{\overline{d^j}}\right) \quad (i \neq j), \tag{4}$$

where t_l^i is the lth spike time of the ith neuron, $\overline{d^j}$ is the mean inter-spike interval (ISI) of the ith neuron, and m runs from 1 to the total number of spikes by neuron j. If the spike train is generated according to a totally random process, the $s_l^{i,j}$ will be uniformly distributed between 0 and 1 (Katori et al., 2010).

To evaluate the above firing feature metrics, we need to consider how to choose the spatiotemporal segments that specify the periods of the spike train and the neuronal groups (neuronal subfractions) for averaging the metrics. The appropriate segment size, i.e., the length of the period and the number of neurons in the segments, were determined according to the dependency of the variation of mean firing rate on the segment size. The temporal FVs were averaged each for the neuronal subfractions ($n = 3$), and the spatial FVs (Eqs. (3) and (4)) were determined for each neuron for combinations with all other neurons, and they were averaged for the individual neuronal subfractions. The frequency histogram of MD values determined for the neuronal subfractions was constructed with the interval of 0.04 (25 bins), normalized so that the sum of histogram values is unity, and used for the feature vectors (MD 1–25 with 0.04 step within the interval [0, 1]). The MD histogram exhibited an even, leftward or rightward skewed distribution depending on whether no interaction existed, or a positive or negative interaction existed, in ensemble neuronal firing. The firing dynamics characterized by the 34 FVs were contracted onto two major PCA axes (see Section 3.3) for search of the best fit between the EXP and SIM spike segments.

2.6. Best-fit search by a juggling algorithm

The g_c and g_i for the SIM spike segments that showed the closest match (the minimum PCA errors) to the EXP spike segments were searched in the PCA space as the solution to the inverse problem to estimate g_c and g_i from the firing dynamics. However, a global search of the best fit with no constraint failed to resolve the inverse problem, due to the ill-posed nature of the inverse problem, because the major determinant of the IO firing dynamics was the g_c/g_i ratio rather than either individual value (Katori et al., 2010; Onizuka, 2009). This issue was resolved by a "juggling algorithm", in which the match between the SIM and EXP spike segments was searched under the constraint that g_c and g_i remain unchanged

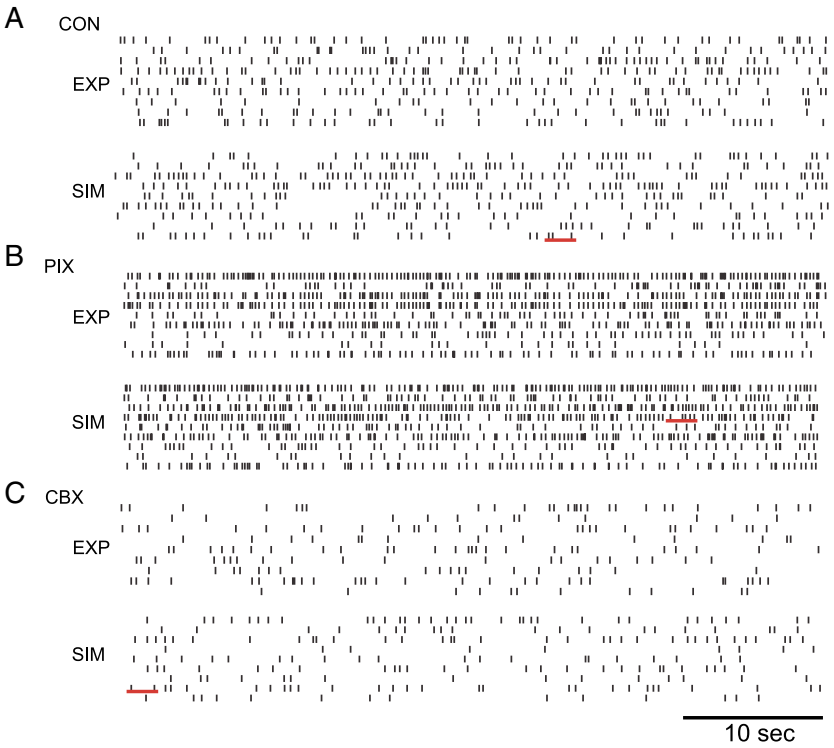

Fig. 2. Raster display of firing in experimental and simulated IO neurons. A–C compare the firing dynamics for the control (CON), picrotoxin (PIX), and carbenoxolone (CBX) conditions between nine pairs of experimental (EXP) and simulation neurons (SIM) of the best fit found in PCA of 34 firing feature vectors. Red bars at the bottom of SIM spike rasters of cells #9, 4, and 8 indicate the periods during which the membrane voltage traces in the spine, dendrite, and soma compartments are shown in Fig. 8.

by PIX and CBX administration, respectively. This constraint was based the experimental facts that PIX's action should reduce g_i but have no effect on g_c, whereas the converse is true for CBX. Therefore, the estimated distributions of g_c should overlap each other between the CON and PIX conditions, and similarly those for g_i in the CON and CBX conditions should overlap.

The juggling algorithm consisted of four steps. First, a global search with no constraint was conducted to find g_i and g_c for CON spike segments sampled in both PIX and CBX experiments. Second, a constrained search was conducted to find the partner g_i that paired with the ensemble g_c for the CON spike segments determined by the global search. Third, a similar constrained search was conducted to find the partner g_c paired with the ensemble g_i for the CON and PIX spike segments in the PIX experiments, determined by the second step search. Fourth, another constrained search was conducted to find the partner g_i paired with the ensemble g_c for the CON and PIX spike segments in the PIX experiments, determined by the third step search. The loop of steps 2–4 was repeated until the ensemble of g_c for PIX experiments matched with that for CON experiments and so was repeated until the ensemble of g_i for CBX experiments matched with that of CON experiments.

3. Results

3.1. Multiple spike trains from experiments

Complex spike (CS) trains (500 s long) were sampled from previously reported experiments in which recordings were obtained from 136 Purkinje cells (PCs) during CON and PIX conditions ($n = 5$ experiments), and from 35 PCs during CON and CBX conditions ($n = 2$, Blenkinsop & Lang, 2006; Lang, 2002; Lang et al., 1996, see Table 1). Fig. 2 illustrates the CS spike trains of nine representative PCs (#1–9) in the CON (for the PIX experiment), PIX, and CBX conditions (upper rasters labeled EXP of Fig. 2(A)–(C)).

Table 1
Experimental data of animals, neurons, and references 500 s long spike data were collected from experimental data and divided into segments of 25 or 50 s. The number of animals, recorded cell numbers, and the original references, from which data were collected, are shown.

Animal no.	EXP condition	Cell	Original reference
1	CBX	22	Blenkinsop and Lang (2006)
2	CBX	13	
3	PIX	16	Lang et al. (1996) and Lang (2002)
4	PIX	25	
5	PIX	42	
6	PIX	32	
7	PIX	21	

The CS activity became much more frequent (50% increase) and oscillatory in the PIX than the CON condition and vice versa (50% decrease in firing frequency) in the CBX condition. Notice also that the firing dynamics significantly fluctuate: dense at certain times and sparse at others. It is important to note that while PC CS activity was recorded in these experiments, CSs bear a one-to-one relationship to IO neuronal spikes, and thus exactly reflect the firing of IO neurons, which allows them to be used as proxies for IO spike trains, and thus we will use the terms CS and IO spike interchangeably.

3.2. Quantitative analysis of multiple spike trains

We fractionized an entire spike train into time segments, and also split the entire IO unit ensemble into neuronal subsets, and estimated the firing feature metrics for each spatiotemporal segment. With an increase in segment size, the metrics became more reliable, but lost their spatiotemporal resolution. So, to choose an appropriate segment size we plotted the variance of the mean spike rate normalized by its square mean as a function of segment duration for the entire neuronal ensemble (Fig. 3(A)).

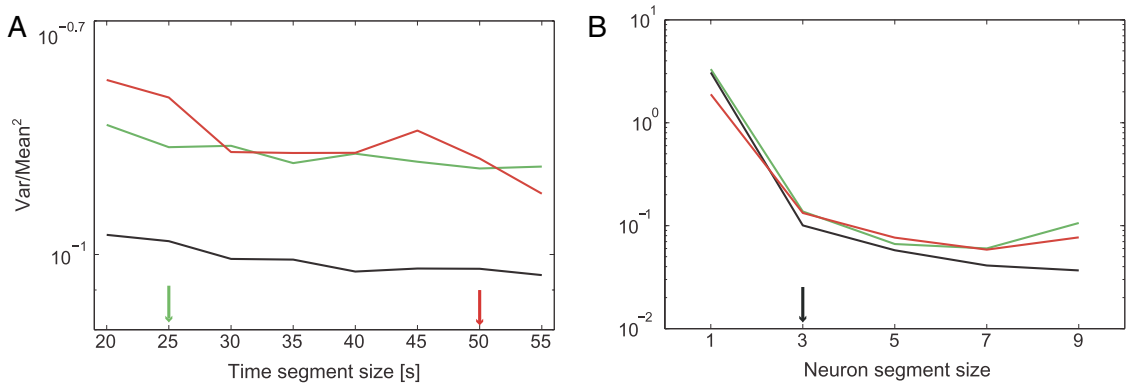

Fig. 3. Relation between variance of firing rates and segmentation of spike train. A and B: for segment length and size of neuronal grouping. Ordinate plots variance of the mean spike rate normalized by the square mean for the six control, four PIX, and two CBX experiments (black, red, and green lines). The abscissa is the size of the spike train segment and the size of neuronal grouping. The same color conventions to represent the three experimental conditions are used in subsequent figures. Green, red, and black arrows indicate the size selected for the segmentation of the spike train.

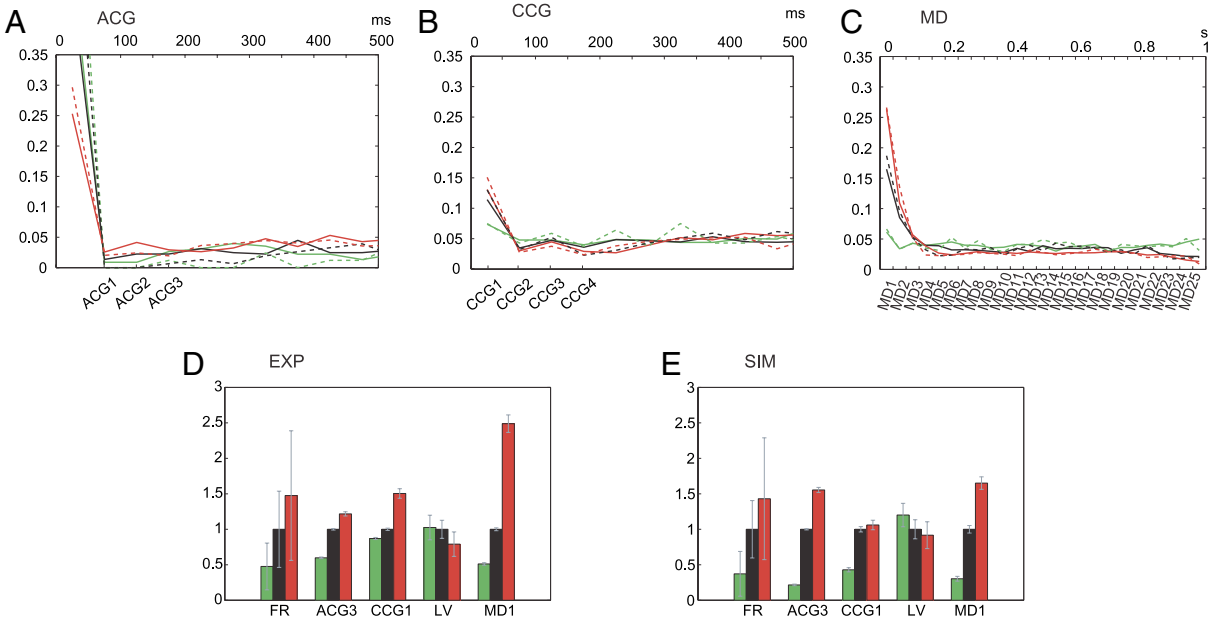

Fig. 4. Three representative feature vectors for three experimental conditions. A–C: auto- and cross-correlogram and minimal distance determined for one spike segment of cell EXP #1 and SIM #1 (solid and dotted lines) in Fig. 2. Feature vectors (FVs) were selected and estimated at the 3, 4, and 25 sampling points in A–C (shown by tick marks). D and E compare the means and SD of the five representative FVs determined for the entire spike segments for the seven control, five PIX, and two CBX experiments and corresponding simulation data. The ordinate of D is scaled so that the control is 1. We note that LVs in the three experimental conditions are all less than 1, which indicates regular spiking.

The normalized variance rapidly decreased for the CBX spike data (green trace) at duration of around 20–25 s, and gradually decreased for the PIX and CON data (red and dark traces) for durations of 20–50 s. Therefore, we selected 25 and 50 s as the segment duration for the CBX (green arrow) and for the PIX and CON (red and dark arrow) data, respectively. Likewise, the normalized variances of the mean spike rate determined for the selected segment duration for PIX, CBX, and CON conditions all decreased with an increase of the size of the neuronal subset (Fig. 3(B)). The rate of this decrease was rapid until subsets had three or more neurons; thus, we selected three neurons as the standard neuronal segment size for PIX, CBX, and CON conditions (dark arrow in Fig. 3(B)).

The IO firing dynamics that varied from cell to cell and from time to time (see Fig. 2) were evaluated by a total of 34 feature vectors (FVs), including the five temporal ones, that is, the firing rate (*FR*), three submetrics of the auto-correlogram (*ACG* 1–3 measure at three characteristic delays, 50–100, 100–150, and 150–200 ms), the local variation (*LV*), and 29 spatial ones, that is, four submetrics of the cross-correlograms measured at four characteristic delays (*CCG* 1–4, at 0–50, 50–100, 100–150, and 150–200 ms), and 25 submetrics of the minimal distance (MD 1–25). The MD metrics exhibit even, leftward and rightward skewed distribution ranging from 0 to 1, in cases when no, positive, and negative interaction exists in the firing of the neuronal ensemble, respectively. Therefore, the MD was measured at many sampling points to capture precise patterns of spatial interaction.

FVs were determined for a total of 440 segments including the five sets of the CON and PIX experiments (10 segments each for 5, 8, 14, 10, and 7 subneuronal ensembles of IO units sampled in five CON and five PIX experiments) and a total of 220 segments including the two sets of CON and CBX experiments (20 segments each for 7 and 4 subneuronal ensembles sampled in two CON and two CBX experiments).

Fig. 4 shows four FVs, including the *ACG* (A), *CCG* (B), and MD (C) for a representative IO unit (#1 in Fig. 2) for PIX, CBX, and CON conditions, and illustrates how three submetrics of the *ACG* (*ACG* 1, 2, 3) and four of the *CCG* (*CCG* 1, 2, 3, 4) and 25 of the

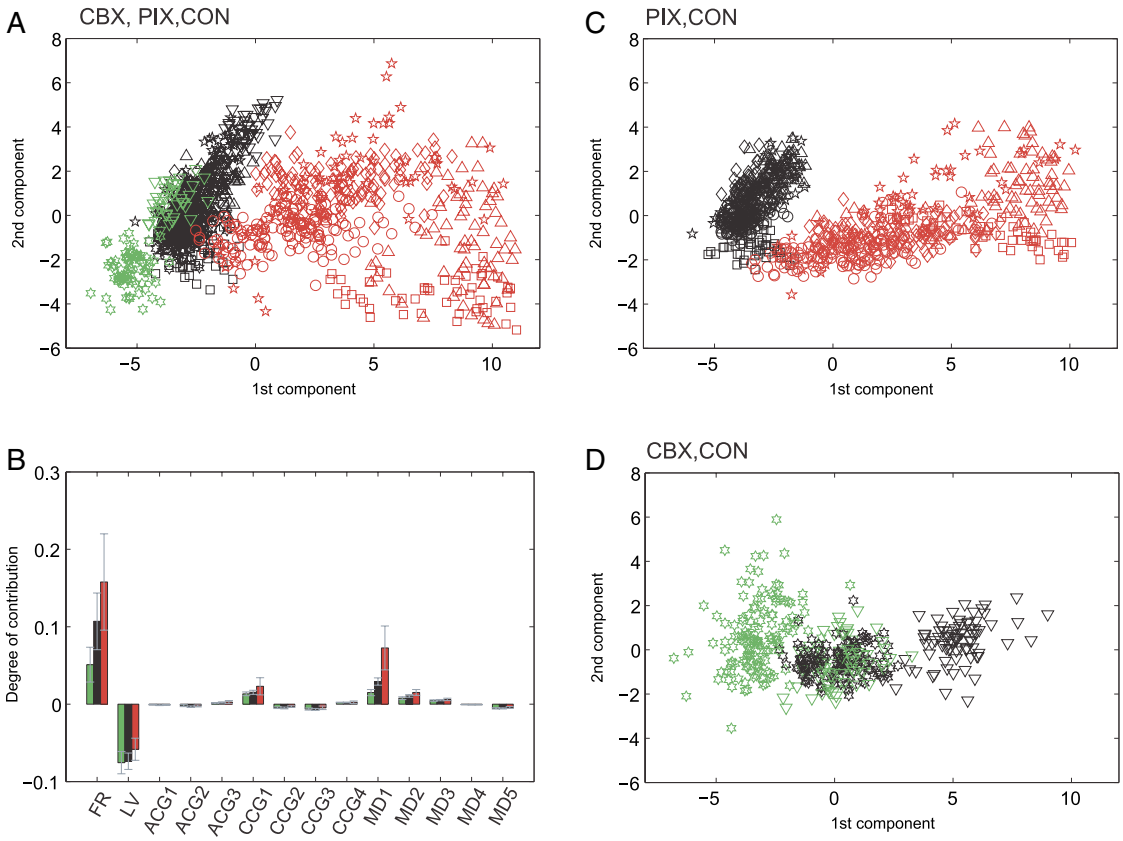

Fig. 5. Scores of three- and two-condition PCAs and contributions of major vectors to first PCA axis. A, C, D: Three-condition PCA for (CON, PIX, and CBX in A) and two two-condition PCAs (CON and PIX in C and CON and CBX in D); each symbol represents PCA score of individual spike segments. B: contributions of selected major 14 feature vectors (FR, LV, ACG1–3, CCG1–4, MD1–5) to the first PCA axis. The mean and SD were computed for all PIX, CON, and CBX spike segments.

MD were evaluated. Fig. 4(D) shows the five representative FVs averaged for 660 CON (for 440 PIX and 220 CBX experiments), 220 CBX, and 440 PIX spike segments each for 55 (44 and 11 for PIX and CBX experiments), 11, and 44 IO unit ensembles, respectively. Four (*FR*, *ACG* 3, *CCG* 1, and MD 1) of the five FVs increased in the PIX and decreased in the CON condition, and vice versa for the CBX condition, whereas *LV* showed the opposite change, being lower in the PIX and higher in the CBX condition. The changes in the FVs elucidate the firing dynamics, which became more frequent, oscillatory, and regular in the individual IO neurons and more synchronous across the IO neuronal ensemble under the PIX than the CON condition, and showed the opposite changes under the CBX condition. Fig. 4(E) shows that the SIM spike data fitted to the EXP ones in the PCA space (see Fig. 6(A) and (B)) rather closely reproduced the changes in FVs for EXP spike data in CON, PIX, and CBX conditions. A relatively low error rate, determined as the difference between the FVs for the EXP and SIM data normalized by the EXP ((SIM–EXP)/EXP), for each FV (0.36 ± 0.24, 0.45 ± 0.44, 0.60 ± 0.43, 0.23 ± 0.15, 0.42 ± 0.33 for *FR*, *ACG* 3, *CCG* 1, *LV*, and MD 1) also confirmed the goodness of the fit between FVs of the EXP and SIM spike train segments.

3.3. Principal component analysis (PCA) of firing feature vectors

We conducted PCA to obtain a simpler measure of the firing dynamics evaluated by the 34 FVs for CON, PIX, and CBX conditions. The calculation of the "variance accounted for" (VAF) indicated that the first two orthogonal components explained a major part (VAF = 0.62) of the firing dynamics (first and second components, 0.51 and 0.11, respectively). The EXP spike segments for the CON, PIX, and CBX conditions formed three clusters along the first PCA axis, with significant overlap between the CON and CBX clusters (Fig. 5(A)). An ANOVA for the three-condition PCA scores also indicated that the separations between the three clusters were extremely significant. (Table 2(A).)

Fig. 5(B) shows the contribution, defined as the product between the FV values and the coefficients of the FVs for the 14

Table 2
ANOVA for firing dynamics of experimental and simulation spike trains under three experimental conditions A–C. The mean and standard deviation of the first principal component scores are shown for PCA for three and two experimental conditions.

(A) ANOVA for CON, PIX, and CBX conditions (first component).

	CON	PIX	CBX
EXP	-2.43 ± 1.03	4.19 ± 3.44	-4.63 ± 1.03
T(PIX, CBX–CON)		-38.97	20.52
		($p = 5.71\text{E}{-154}$)	($p = 3.13\text{E}{-46}$)
F(SIM–EXP)	4.49E−04 ($p = 0.98$)		

(B) ANOVA for CON and PIX conditions (first component).

	CON	PIX
EXP	-3.30 ± 0.87	3.30 ± 3.44
SIM	-3.30 ± 0.87	3.30 ± 3.44
F(PIX–CON)	3043.8 ($p < 0.0001$)	
F(SIM–EXP)	1.33E−04 ($p = 0.99$)	

(C) ANOVA for CON and CBX conditions (first component).

	CON	CBX
EXP	1.96 ± 2.67	-1.96 ± 1.97
SIM	1.93 ± 2.65	-1.96 ± 1.97
F(CBX–CON)	613.28 ($p = 4.76\text{E}{-103}$)	
F(SIM–EXP)	0.0082 ($p = 0.92$)	

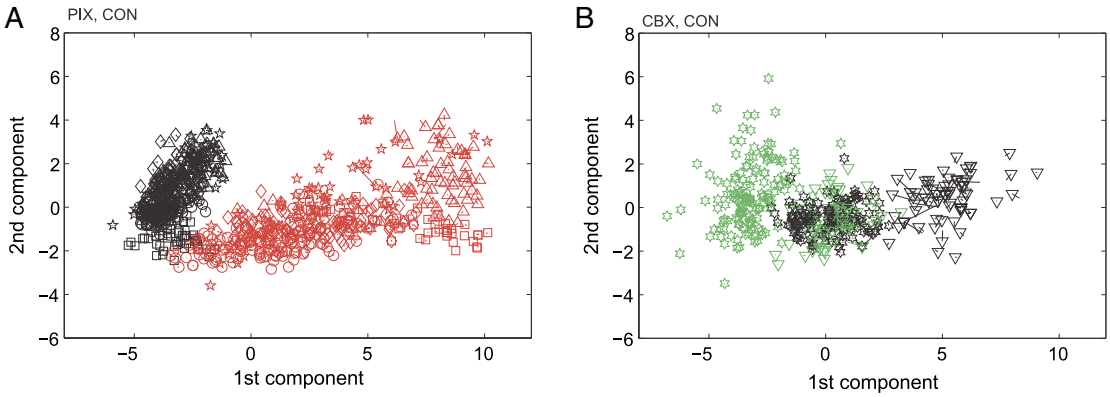

Fig. 6. PCA errors between experimental and simulation spike segments. A and B correspond to Fig. 5(C) and (D). Each symbol here represents an SIM spike segment. The bar represents PCA error and therefore the end of the bar represents the PCA score of the corresponding SIM spike segments.

major FVs to the first PCA component. The major contributors to the PCA scores, such as *FR*, *ACG* 3, *CCG* 1, and MD 1, were positive except for *LV*, which was negative, and were largest for PIX and smallest for CBX, and vice versa for *LV*. This finding is consistent with the locations of EXP spike segment clusters for CON (middle), PIX (rightmost), and CBX (leftmost) conditions in Fig. 5(A), and also the changes of the FVs for those conditions in Fig. 4(D). All of these findings consistently indicate that IO firing becomes higher, more regular, oscillatory, and synchronous across the IO neuronal ensemble under the PIX than the CON condition, and vice versa under the CBX condition.

ANOVA for the three-condition PCA (Table 2(A)) indicated a close match between EXP and SIM spike segments ($p = 0.98$), and a marked separation of CON, PIX, and CBX clusters ($p < 10^{-40}$). However, we considered that the global search of the match in the three-condition PCA space was insufficient for two reasons. First, visual inspection indicated a significant overlap between CON and CBX spike segments (see Fig. 5(A)). Therefore the PCA space should be optimized for better separation of CON and CBX data clusters. Second, the match in the PCA space failed to give correct estimates of the inhibitory conductance (g_i) and gap-junctional conductance (g_c) due to the ill-posed nature of the inverse problem that the firing dynamics depend on the ratio of g_i to g_c rather than the individual values.

This problem was resolved by conducting two separate two-condition PCAs each for CON and PIX, and for CON and CBX clusters, and a juggling search for the best fit between EXP and SIM spike segments across the two PCA spaces (see Model parameter estimation). The 34 FVs for the CON and PIX spike segments were ranked by t-values of the t-test, and the top 25 FVs were used for two-condition PCA. Fig. 5(C) shows the results of two-condition PCA, indicating that the separations between the PIX and CON clusters are significantly improved. The two-condition PCA with the 25 FVs also produced a significant improvement of separation between the CBX and CON clusters (Fig. 5(D)).

3.4. Model parameter estimation

We generated SIM spike data of the same number and the same length of the spike segments for the CON, PIX, and CBX conditions (see Method). We mapped them onto the two PCA spaces for EXP spike data for CON–PIX and CON–CBX conditions, respectively, and conducted a global search for the best fit with the minimal PCA error between the SIM and EXP spike segments evaluated in the two-dimensional axes of PCA. Global search of the best fit in the two-condition PCA for CON and PIX, and that for CON and CBX spike segments both failed to give estimates of g_i that match between CON and CBX conditions, and so did those of g_c between CON and PIX conditions, respectively. This is the requirement from the neuroscience studies that PIX depresses g_i but not g_c, and vice versa for CBX. The mismatch of g_i and g_c between the two control conditions was due to the fact that IO firing dynamics depend on the shunting conductance determined by a ratio of g_c to g_i rather than the individual values. We resolved this problem by conducting a juggling search for the best fit in the two PCA spaces. That is, PIX · g_cs and CBX · g_is were jointly estimated in combination with PIX · g_is and CBX · g_cs while assuming that the PIX · g_cs overlap with CON · g_cs and so CBX · g_i with CON · g_i (Method 2.6). We continued the juggling search until the difference of mean g_i and g_c became statistically insignificant between the two CON conditions ($p > 0.5$) by a t-test. Fig. 6(A) and (B) show the results after the juggling searches (number of iteration = 3) between the CON–PIX and CON–CBX spaces, where the PCA errors were plotted as bars extending from the symbols representing the PCA scores of the SIM spike segments. Generally, the errors were almost invisibly small, except for a relatively few plots of the CON–PIX and CON–CBX spaces (those in the upper-right quadrant of Fig. 6(A) and in the central part of Fig. 6(B)). The average error rate of the PCA scores estimated as (SIM–EXP)/EXP for SIM spike segments was all very low for CON, PIX, and CBX conditions (0.02, 0.025, and 0.02). Visual comparison of the raw EXP and SIM spike data for the three conditions also revealed a fine match (see upper and lower spike segments in Fig. 2(A)–(C)). Although the individual SIM spikes were not those exactly corresponding to the EXP spikes, they finely reproduced the spatiotemporal features of firing such as the frequency, oscillation, burstiness, and synchrony under the three EXP conditions. The five major FVs (FR, ACG3, CCG1, LV, and MD1) for representatives of SIM spikes were in general fine match with the FVs for those of EXP spikes (see solid and dotted traces in Fig. 4(A)–(C), see also D and E). The error rates of the FVs were also rather low.

The performance of the juggling search between the two PCA spaces was also confirmed by ANOVA. The difference in the first principal component scores was highly significant between the CON and PIX spike segments (Table 2(B)) or between those of the CON and CBX conditions (Table 2(C)), but insignificant between the SIM and EXP ones. The error rates of SIM with EXP spike segment in the two-condition PCA spaces were two orders of magnitude smaller than those for the conventional mean-based match (2.09, 1.88, and 2.34 for CON, PIX, and CBX conditions) that minimized the PCA errors for the mean of the entire spike segment for the entire neuronal ensemble.

Fig. 7(A) and (B) plot the frequency histograms of g_is and g_cs estimated as those for the spike segments of the best fit with the EXP spike segments, determined by the juggling search. The g_i values for the CON and CBX conditions showed a rather

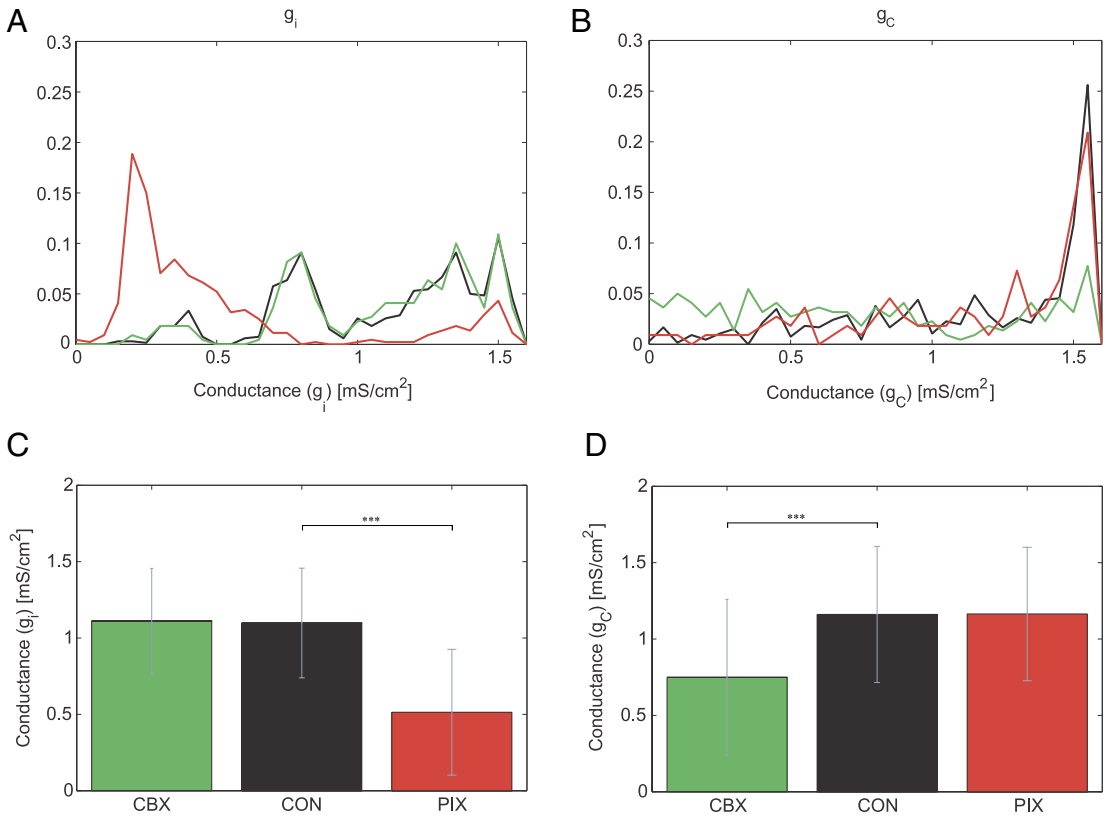

Fig. 7. Estimates of inhibitory and gap junction conductance. A and B: frequency histograms of g_i and g_c determined by a juggling search. Each histogram is normalized for the subpopulation of CON, PIX, or CBX spike segments ($n = 660$, 440, and 220). C and D, the mean and SD of inhibitory and gap-junctional conductances for the three experimental conditions. The triple asterisk indicates statistical significance $p < 0.05$.

wide distribution around 1 mS/cm^2 overlapping each other, while those for the PIX condition showed a rather sharp distribution around 0.3 mS/cm^2. Conversely, the g_c values for the CON and PIX conditions exhibited a sharp and overlapped distribution around 1.5 mS/cm^2, while those for the CBX condition showed a wide distribution extending over the entire range of simulation. Fig. 7(C) and (D) show the mean and SD for g_i and g_c for the three EXP conditions. g_i was reduced under the PIX condition to roughly a half (0.51 ± 0.41 mS/cm^2) of that for the CON condition (1.10 ± 0.36 mS/cm^2) and remained unchanged for the CBX condition (1.11 ± 0.34 mS/cm^2). Likewise g_c was decreased under CBX condition to roughly two-thirds (0.75 ± 0.51 mS/cm^2) of that for the CON condition (1.16 ± 0.44 mS/cm^2) and remained unchanged under the PIX condition (1.16 ± 0.44 mS/cm^2).

3.5. Robustness analysis

The firing dynamics of the IO network model may depend on a number of parameters such as the excitatory synaptic conductance g_e, besides the critical parameters g_i and g_c whose effects on IO firing were systematically studied in the present study. To show the robustness of the present results, we conducted simulations in which parameter g_e was 10% larger or smaller than the standard ones. ANOVA of scores of the SIM spike segments in the two-condition PCA for CON–PIX and for CON–CBX revealed no significant difference across a $\pm 10\%$ change of g_e from the baseline ($p = 0.99$ and 0.96). Therefore, the firing dynamics did not change significantly across the three conditions, and the g_i and g_c estimates were robust for the changes in g_e.

3.6. Voltage-trace reconstruction

Fig. 8 illustrates voltage traces for parts of raster plots shown in Fig. 2 (see red bars shown at the bottom of spike rasters). There were full-sized narrow spikes in the soma segment and small-sized spikes in the dendrite and spine compartments that represented Na spikes initiated in the soma and electronically transmitted to the dendrite and spines in most of the spike segments under all of the CON, PIX, and CBX conditions (Fig. 8(A)–(I)). In rather rare cases (17, 14, and 16 spikes each for 3600 spike segments under CON, PIX, and CBX conditions), we found a full-sized broad spike in the spine and dendrite compartments and a smaller one in the soma compartment that represented Ca spikes initiated in the dendrite and transmitted to the soma and spines, and a few Na spikes initiated in the soma following the Ca spike (Fig. 8(J)–(L)). There was a tendency that the baseline negative membrane potential was deepest, modest, and shallowest for CBX, CON, and PIX conditions across the spine, dendrite, and soma compartments ($p < 10^{-100}$ by ANOVA for 400 spike segments). Correspondingly, the baseline noise estimated as RMS was largest, modest, and smallest for CBX, CON, and PIX conditions ($p < 10^{-100}$). The baseline was most oscillatory in the PIX condition and most quiescent in the CBX condition. All of these findings are consistent with those for FVs of EXP and SIM spike segments (see Fig. 4(D) and (E)).

4. Discussion

The spatiotemporal dynamics of IO firing have been studied by multi-channel recording as the climbing fiber responses (complex spikes) in cerebellar Purkinje cells under pharmacological suppression of the cerebellar nuclear inhibition by PIX and gap-junctional

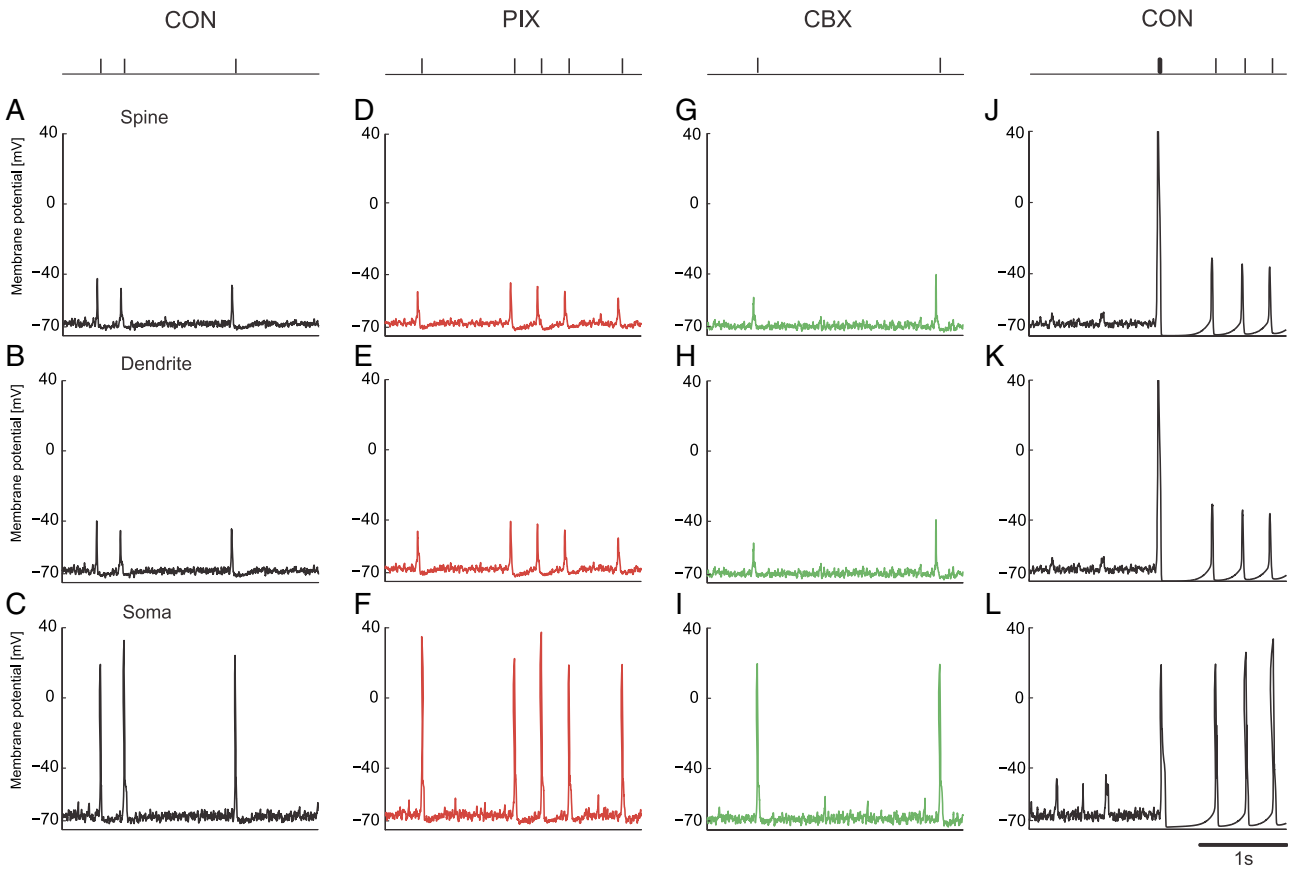

Fig. 8. Voltage trace for spike segments. A, B and C: traces of membrane potential in the spine, dendrite, and soma compartments of cell #9 for a part of the SIM spike train under the CON condition (a red bar) shown in Fig. 2. D–F, G–J, and J–L: similar traces to A–C under PIX, CBX, and CON conditions for cells #4, 8, and 1, respectively.

connectivity by CBX (Blenkinsop & Lang, 2006; Lang, 2002; Lang et al., 1996). IO firing became more frequent and regular in the individual neurons and more synchronized across the neurons under the PIX application and vice versa under the CBX application. It was previously hypothesized that these changes were in large part due to modulation of the effective coupling conductance between IO neurons. Specifically, PIX, by acting as a GABA-A receptor antagonist, increased the effective conductance between IO neurons by reducing the shunting inhibition that occurs when GABA binds to its receptors. Moreover, CBX decreased the effective conductance by directly causing a decrement of the gap-junctional conductance.

Our study aimed to test these hypotheses by resolving the inverse problem to estimate the synaptic conductance from the neuronal firing, using an IO network model as the forward model for Bayesian inference. The network model generated spike data for step-wise variations of the model parameters, g_i and g_c, and the solutions were found as those giving the SIM spike data that was best fitted to the EXP spike data. There were three difficulties in this approach. The first problem was how to find the match of the simulation spike data with the EXP ones that convey complicated firing dynamics, varying in space (from neuron to neuron) and time. We resolved this issue by fractionating the spike data into spatiotemporal segments (short spike segments for small neuronal ensembles) and searching for the match for every segment. The segment-wise fitting is expected to increase the degrees of freedom for fitting. In fact, we found that the error rate of the segment-wise fitting in the PCA space was two orders of magnitude smaller compared with that for the conventional mean-based fitting. The second difficulty was how to evaluate the complicated dynamics of IO firing and compare between EXP and SIM spike data. This problem was resolved by evaluating the spatiotemporal dynamics of IO firing by a multitude of firing feature metrics, contracting them onto the two-dimensional PCA space and finding the match as the pairs of EXP and SIM spike segments that convey the minimum distance in the PCA space. The third difficulty was the ill-posed nature of the inverse problem due to the fact that IO firing depends on the shunting conductance defined by a ratio of g_c to g_i rather than the individual values. This problem was resolved by a juggling search where the best fit was found under the constraint that g_c remains unchanged between CON and PIX conditions and so does g_i between CON and CBX conditions.

Our method to resolve the inverse problem may be equivalent to Bayesian estimation of the model parameters using simulation as the forward model. The global and juggling search algorithms may roughly correspond to Bayesian estimation of CON $\cdot$ g_c, CON $\cdot$ g_i and PIX $\cdot$ g_i, CBX $\cdot$ g_c with no prior information and with the prior information that PIX $\cdot$ g_c $=$ CON $\cdot$ g_c and CBX $\cdot$ g_i $=$ CON $\cdot$ g_i, respectively. One of our future studies is to utilize a more general method to approximate the likelihood distribution, which determines the firing pattern probability from a given set of parameter values. One possible way is to use a finite temperature in the Gibbs distribution rather than zero temperature, corresponding to the present method in picking up only the closest parameter. Function approximation of the likelihood or non-parametric approach is another possibility for Bayesian estimation.

Visual inspection of representative EXP and SIM spike segment pairs, statistical analysis of all EXP–SIM data by ANOVA, and error rate analysis all indicated a fine match between EXP and SIM spike data and substantiated the reliability of our analysis. The voltage traces for SIM spikes demonstrated the membrane events in the soma consistent with the findings of FVs for the SIM spikes, such as the deepest and most noisy baseline membrane potential for the

CBX condition, and the most oscillatory and least noisy baseline for the PIX condition. Our IO network model introduced all the known neuronal and network structures, such as soma, dendrite, spines with gap junctions, and the excitatory and inhibitory synaptic inputs impinging on these neuronal structures. The inhibitory synapses and dendritic spines containing gap junctions were not modeled in previous theoretical IO studies. The precision of our model to reproduce the IO circuitry to the subcellular level, and the findings that are consistent across different levels of observation including voltage traces, raw firing patterns, FVs of the firing, and the PCA transform for the three experimental conditions, strengthens the conclusion of our analysis.

Our analysis indicates that g_i and g_c were reduced to roughly 50% and 70% of their control values under the PIX and CBX conditions, respectively. It is significant that g_i and g_c are almost equal under the CON conditions (1.10 ± 0.36 and 1.16 ± 0.44 mS/cm^2), which is optimal for them to act in changing effective conductance for the interneuronal crosstalk. Correspondingly, the effective coupling conductance evaluated by utilizing the formula of Katori et al. (2010) and Onizuka (2009) increased by 110% under the PIX condition compared with the CON condition, and decreased by 34% under the CBX condition compared with the CON condition. The results indicated that the inhibition opposed to the gap-junctional coupling is a very effective device to control the IO neuronal crosstalk. The decrease of g_i increases the effective coupling conductance, allowing greater interneuronal crosstalk, and consequently the IO firing becomes more frequent, regular, oscillatory, and synchronous. This is exactly what is shown by the changes in the major FVs of the EXP data of IO firing: an increase in FR, ACG3, CCG1, and MD1, and a decrease in LV in Fig. 4(D). This would also be the case if the Purkinje cells were more active and the DCN cells became suppressed and exerted weaker inhibition on the IO neurons and induced the same changes as for the PIX case.

These findings are consistent with the view that the DCN inhibition of IO neurons may work as a decoupling device (Best & Regehr, 2009; Lang et al., 1996; Llinás & Sasaki, 1989) and the role of the DCN on complex spike firing patterns (De Zeeuw et al., 2011). In addition, our findings are also consistent with the hypothesis that the closed-loop circuit across PC, DCN, IO, and back to PC optimizes the degrees of freedom of the cerebellar learning system (roughly the number of independent variables in the learning system) as detailed below (Kawato, Kuroda, & Schweighofer, 2011). That is, in the early phase of motor learning, when motor acts are clumsy and far from the desired ones and the executed movement trajectories are perturbed, the motor plans and commands need to be grossly modulated. Conversely, in the late phase of the learning, when the motor acts become skillful and the movement trajectories are smooth and close to the desired ones, the motor plans and commands need to be finely tuned. The neural events to meet these motor-learning requirements would be massive mossy- and climbing-fiber inputs to the PCs in the early phase of the motor learning, and small mossy- and climbing-fiber inputs in the late phase. The PC–DCN–IO circuits through which PCs inhibit DCN and DCN inhibit IO may act as machinery for the neural events to satisfy the motor-learning requirements. If PCs are more active in the early phase of the motor learning due to massive mossy-fiber inputs to be learned by the PCs, DCN become less active, and the IO neurons become active and send stronger error signals to the PCs. The opposite may be the case in the late phase of learning.

High effective coupling across the IO neurons due to low inhibition during the early learning phase would reduce the dimension and increase the amplitude of the error signals for rough and fast motor learning, and vice versa during the late phase for fine and slow learning. The mosaic structures of the cerebellar system where the IO–PC–CN loop is topographically organized (micro-complex in Ito, 1984 and Marshall & Lang, 2009) may help the dimensional control of motor learning. If many PCs fire synchronously and change their firings in the early phase of learning, as instructed by the massive IO error signals of small number of degrees of freedom, PC learning would be fast but coarse. Conversely in the late phase of learning, the PCs and IO neuronal firing become less synchronized and may even become chaotic (Schweighofer et al., 2004), expanding the degrees of freedom for fine but slow PC learning.

Acknowledgments

This study is a result of the "Brain Machine Interface Development" carried out under the Strategic Research Program for Brain Sciences by the Ministry of Education, Culture, Sports, Science and Technology of Japan (MEXT). IT was supported by Grants-in-Aid for Scientific Research (C) (No. 23560446) from MEXT of Japan. HH was supported by an ASTER scholarship. NS was supported by grant NSF BCS-1031899. YK and KA were supported by the Aihara Innovative Mathematical Modeling Project, the Japan Society for the Promotion of Science (JSPS) through its "Funding Program for World-Leading Innovative R&D on Science and Technology (FIRST Program). EJL was supported by grant NSF IOS-1051858. MO and KT were supported by a contract with the National Institute of Information and Communications Technology entitled 'Multimodal integration for brain imaging measurements'.

Appendix

The membrane potential of the soma, dendrite, and spine compartments (V_o, V_d and V_p) was calculated as follows.

$$\text{soma: } C_m \frac{dV_o}{dt} = -\sum (I_{\text{Na}} + I_{\text{K}} + I_{\text{Cal}} + I_h + I_{lo} + I_{do} + I_{\text{synapse}}), \tag{A.1}$$

$$\text{dendrite: } C_m \frac{dV_d}{dt} = -\sum \left(I_{\text{Cah}} + I_{\text{KCa}} + I_{od} + I_{ld} + \sum_{i=1}^{4} [I_{pd}]_i + I_{\text{synapse}} \right), \tag{A.2}$$

$$\text{spine: } C_m \frac{d[V_p]_i}{dt} = -\sum (I_C + I_{lp} + I_{dp} + I_{\text{synapse}}). \tag{A.3}$$

Soma compartment

The structures of the soma compartment exactly followed those of Schweighofer et al. (2004). The change of somatic membrane potential V_o, which is proportional to the sum of I_{Na}, I_{K}, I_{Cal}, I_h, I_{lo}, I_{do}, and I_{synapse} that consists of I_e and I_i, is as follows:

$$C_m \frac{dV_o}{dt} = -\sum (I_{\text{Na}} + I_{\text{K}} + I_{\text{Cal}} + I_h + I_{lo} + I_{do} + I_{\text{synapse}}),$$

where C_m is the membrane capacitance 1 μF/cm^2, and I_{Na}, I_{K}, I_{Cal}, I_{h}, I_{lo}, and I_{synapse} are the currents across ionic conductances g_{Na}, g_{K}, g_{Cal}, g_h, g_o, g_e, and g_i. The parameter values used in the simulation are summarized in Table A.1.

I_{Na} is given by the Hodgkin–Huxley-type inward sodium current as

$$I_{\text{Na}} = g_{\text{Na}} m_\infty (V_o - E_{\text{Na}}) \tag{A.4}$$

$$m_\infty(V_o) = \frac{\alpha_m(V_o)}{\alpha_m(V_o) + \beta_m(V_o)},$$

$$\alpha_m(V_o) = \frac{0.1(V_o + 41)}{1 - \exp[-(V_o + 41)/10]},$$

Table A.1
List of parameters used for simulation and references.

Parameter	Value	Ref. no.
g_{Na}	70.0 mS/cm^2	Schweighofer et al. (1999)
g_K	18.0 mS/cm^2	Schweighofer et al. (1999)
g_{Cal}	2.0 mS/cm^2	Schweighofer et al. (2004)
g_h	0.15 mS/cm^2	Schweighofer et al. (2004)
g_s	0.015 mS/cm^2	Schweighofer et al. (1999)
g_{Cah}	4.0 mS/cm^2	Schweighofer et al. (1999)
g_{KCa}	35.0 mS/cm^2	Schweighofer et al. (1999)
g_d	0.015 mS/cm^2	Schweighofer et al. (1999)
g_p	0.015 mS/cm^2	Schweighofer et al. (1999)
g_e	0.03 mS/cm^2	Schweighofer et al. (2004)
$G^{soma,dendrite}/S$	0.13 mS/cm^2	Schweighofer et al. (1999)
$G^{dendrite,spine}/S$	0.1 mS/cm^2	$g_{sd} = 0.1$–3 (Schweighofer et al., 1999), $g_{dp} \leq g_{sd}$
E_{Na}	55 mV	Schweighofer et al. (1999)
E_K	−75 mV	Schweighofer et al. (1999)
E_{Ca}	120 mV	Schweighofer et al. (1999)
E_h	−43 mV	Schweighofer et al. (1999)
E_l	10 mV	Schweighofer et al. (1999)
p	0.14	The ratio of the somatic area to total
q	0.05	surface area: 0.1–0.4 (Manor et al., 1997)

$$\beta_m(V_o) = 9.0\exp\left[-(V_o+66)/20\right],$$
$$h_\infty(V_o) = \frac{\alpha_h(V_o)}{\alpha_h(V_o)+\beta_h(V_o)},$$
$$\tau_h(V_o) = \frac{170}{\alpha_h(V_o)+\beta_h(V_o)},$$
$$\alpha_h(V_o) = 5.0\exp\left[-(V_o+60)/15\right],$$
$$\beta_h(V_o) = \frac{V_o+50}{1-\exp\left[-(V_o+50)/10\right]}.$$

The outward delayed rectifier potassium current I_K is described by

$$I_K = g_K n^4 (V_o - E_K), \tag{A.5}$$
$$n_\infty(V_o) = \frac{\alpha_h(V_o)}{\alpha_h(V_o)+\beta_h(V_o)},$$
$$\tau_n(V_o) = \frac{5}{\alpha_h(V_o)+\beta_h(V_o)},$$
$$\alpha_n(V_o) = \frac{V_o+41}{1-\exp\left[-(V_o+41)/10\right]},$$
$$\beta_m(V_o) = 12.5\exp\left[-(V_o+51)/80\right].$$

The low-threshold calcium inward current I_{Cal} is described by

$$I_{Cal} = g_{Cal} k^3 l\,(V_o - E_{Ca}), \tag{A.6}$$
$$k_\infty(V_o) = \frac{1}{1+\exp\left[-(V_o+61)/4.2\right]}, \qquad \tau_k(V_o) = 1.0,$$
$$l_\infty(V_o) = \frac{1}{1+\exp\left[(V_o+85.5)/8.5\right]},$$
$$\tau_l(V_o) = \frac{20\exp\left[(V_o+160)/30\right]}{1+\exp\left[(V_o+84)/7.3\right]} + 35.$$

The anomalous inward rectifier current I_h is described by

$$I_h = g_h q (V_o - E_h), \tag{A.7}$$
$$q_\infty(V_o) = \frac{1}{1+\exp\left[(V_o+75)/5.5\right]},$$
$$\tau_q(V_o) = \frac{1}{\exp[-0.086V_o - 14.6] + \exp[0.07V_o - 1.87]}.$$

The leakage current I_{lo} is described by

$$I_{lo} = g_o(V_o - E_l). \tag{A.8}$$

The current I_{do} flowing from the dendritic compartment to the somatic compartment is given by

$$I_{do} = g_{do}(V_o - V_d) = \left(G^{soma,dendrite}/p\cdot s\right)(V_o - V_d). \tag{A.9}$$

Here, $G^{soma,dendrite}$ is the actual soma–dendritic inter-compartmental conductance in mS. s is the total surface area of a single neuron. The value of $G^{soma,dendrite}/s$ is given in Table A.1.

Dendritic compartment

The structure of the dendritic compartment was the same as Schweighofer's model except that the gap junction was moved to the spine compartment, and its membrane potential (V_d) obeys the following differential equation:

$$C_m \frac{dV_d}{dt} = -\sum\left(I_{Cah} + I_{KCa} + I_{od} + I_{ld} + \sum_{i=1}^{4}[I_{pd}]_i + I_{synapse}\right).$$

The high-threshold inward calcium current I_{Cah} through g_{Cah} is given by

$$I_{Cah} = g_{Cah} r^2 (V_d - E_{Ca}), \tag{A.10}$$
$$r_\infty(V_d) = \frac{\alpha_r(V_d)}{\alpha_r(V_d)+\beta_r(V_d)}, \qquad \tau_k(V_d) = \frac{1}{\alpha_r(V_d)+\beta_r(V_d)},$$
$$\alpha_r(V_d) = \frac{1.6}{1+\exp\left[-(V_d-5)/13.9\right]},$$
$$\beta_r(V_d) = \frac{0.02(V_d+8.5)}{\exp\left[(V_d+8.5)/5\right]-1}.$$

The outward calcium-dependent potassium current I_{KCa} through g_{KCa} is given by

$$I_{KCa} = g_{KCa} s (V_d - E_K), \tag{A.11}$$
$$s_\infty([Ca^{2+}]) = \frac{\alpha_s([Ca^{2+}])}{\alpha_s([Ca^{2+}])+\beta_s([Ca^{2+}])},$$
$$\tau_s([Ca^{2+}]) = \frac{1}{\alpha_s([Ca^{2+}])+\beta_s([Ca^{2+}])},$$
$$\alpha_s([Ca^{2+}]) = \min(0.00002[Ca^{2+}], 0.01), \qquad \beta_s(V_d) = 0.015,$$
$$\frac{ds}{dt} = \frac{s_\infty([Ca^{2+}]) - s)}{\tau_s([Ca^{2+}])},$$
$$\frac{d[Ca^{2+}]}{dt} = I_{Cah} - 0.02[Ca^{2+}].$$

The leakage current I_{ld} through g_d is given by

$$I_{ld} = g_d(V_d - E_l). \tag{A.12}$$

The inter-compartmental current flowing from the somatic compartment to the dendritic compartment I_{od} is given by

$$I_{od} = g_{od}(V_d - E_o) = \left[G^{soma,dendrite}/(1-p-q)\cdot s\right](V_d - V_o), \tag{A.13}$$

where p is the ratio of the somatic area to the total surface area and q is the ratio of the total of the four spine surface area to the total surface area. The inter-compartmental current flowing from the ith ($i = 1, 2, 3, 4$) spine compartment to the dendritic compartment I_{pd} is given by

$$[I_{pd}]_i = g_{pd}(V_d - [V_p]_i) = \left[G^{dendrite,spine}/(1-p-q)\cdot s\right](V_d - [V_p]_i) \quad (i = 1, 2, 3, 4). \tag{A.14}$$

Spine compartment

The spine compartment is added in our IO neuron model. In the spine compartment, the IO neurons lie next to each other and are coupled by I_C as follows:

$$C_m \frac{d[V_p]_i}{dt} = -\sum (I_C + I_{lp} + I_{dp} + I_{\text{synapse}}).$$

The current flowing into other cells through electrical coupling I_C is given by

$$[I_C]_i = g_c([V_p]_i - V_{p\_\text{next}}). \tag{A.15}$$

The leakage current I_{lp} is described by

$$[I_{lp}]_i = g_p([V_p]_i - V_l). \tag{A.16}$$

The inter-compartmental current flowing from one of the spine compartments to the dendritic compartment I_{dp} is given by

$$\begin{aligned}[I_{dp}]_i &= g_{dp}([V_p]_i - V_d) \\ &= \left[G^{\text{dendrite,spine}}/0.25q \cdot s\right]([V_p]_i - V_d).\end{aligned} \tag{A.17}$$

Synaptic inputs

All of the soma, dendritic, and spine compartments receive the excitatory and inhibitory synaptic inputs driven by the Poisson spike generators of the mean firing rate 10 Hz (Schweighofer et al., 2004), The number of excitatory and inhibitory synapses is 10, 80, and 10 for the soma, dendrite, and spine compartments, respectively, driven by Poisson process spike generators defined as

$$\begin{aligned}I_{\text{syn}}(t) &= \sum_l g_{\text{syn}}(t - t_l)(V - E_{\text{syn}}) \\ g_{\text{syn}}(t) &= \begin{cases} 0 \\ g_{\text{synm}} \cdot t \cdot e^{1 - t/t^{\text{peak}}}, \end{cases}\end{aligned} \tag{A.18}$$

where t_l is the time of the lth spike time, $E_{\text{syn}} = -10$ or -75 mV, and $g_{\text{syn}} = g_e$ or g_i for the inhibitory and excitatory synapses, respectively. The hyperpolarizing constant current of Schweighofer's model was replaced by the inhibitory synaptic inputs in our model.

References

Best, A., & Regehr, W. (2009). Inhibitory regulation of electrically coupled neurons in the inferior olive is mediated by asynchronous release of GABA. *Neuron*, *62*, 555–565.

Blenkinsop, T. A., & Lang, E. J. (2006). Block of inferior olive gap junctional coupling decreases Purkinje cell complex spike synchrony and rhythmicity. *Journal of Neuroscience*, *26*(6), 1739–1748.

De Zeeuw, C. I., Hoebeek, F. E., Bosman, L. W., Schonewille, M., Witter, L., & Koekkoek, S. K. (2011). Spatiotemporal firing patterns in the cerebellum. *Nature Reviews Neuroscience*, *12*(6), 327–344.

De Zeeuw, C. I., Holstege, J. C., Ruigrok, T. J. H., & Voogd, J. (1989). Ultrastructural study of the GABAergic, cerebellar, and mesodiencephalic innervation of the cat medial accessory olive: anterograde tracing combined with immunocytochemistry. *Journal of Comparative Neurology*, *284*, 12–35.

Hirata, Y., & Aihara, K. (2009). Representing spike trains using constant sampling intervals. *Journal of Neuroscience Methods*, *183*, 277–286.

Ito, M. (1984). *The cerebellum and neural control*. New York: Raven Press.

Katori, Y., Lang, E. J., Onizuka, M., Kawato, M., & Aihara, K. (2010). Quantitative modeling of spatio-temporal dynamics of inferior olive neurons with a simple conductance-based model. *International Journal of Bifurcation and Chaos*, *20*(3), 583–603.

Kawato, M., Kuroda, S., & Schweighofer, N. (2011). Cerebellar supervised learning revisited: biophysical modeling and degrees-of-freedom control. *Current Opinion in Neurobiology*, *21*, 791–800.

Lang, E. J. (2002). GABAergic and glutamatergic modulation of spontaneous and motor-cortex-evoked complex spike activity. *Journal of Neurophysiology*, *87*, 1993–2008.

Lang, E. J., Sugihara, I., & Llinás, R. (1996). GABAergic modulation of complex spike activity by the cerebellar nucleoolivary pathway in rat. *Journal of Neurophysiology*, *76*, 255–275.

Lang, E. J., Sugihara, I., Welsh, J. P., & Llinás, R. (1999). Patterns of spontaneous Purkinje cell complex spike activity in the awake rat. *Journal of Neuroscience*, *19*, 2728–2739.

Llinás, R., Baker, R., & Sotelo, C. (1974). Electrotonic coupling between neurons in cat inferior olive. *Journal of Neurophysiology*, *37*, 560–571.

Llinás, R., & Sasaki, K. (1989). The functional organization of the olivo-cerebellar system as examined by multiple Purkinje cell recordings. *European Journal of Neuroscience*, *1*, 587–602.

Llinás, R., & Yarom, Y. (1981). Electrophysiology of mammalian inferior olivary neurones in vitro. Different types of voltage-dependent ionic conductances. *Journal of Physiology*, *315*, 549–567.

Manor, Y., Rinzel, J., Segev, I., & Yarom, Y. (1997). Low-amplitude oscillations in the inferior olive: a model based on electrical coupling of neurons with heterogeneous channel densities. *Journal of Neurophysiology*, *77*, 2736–2752.

Marshall, S. P., & Lang, E. J. (2009). Local changes in the excitability of the cerebellar cortex produce spatially restricted changes in complex spike synchrony. *Journal of Neuroscience*, *29*(45), 14352–14362.

Onizuka, M. (2009). The effect of inhibitory synaptic input on glomeruli in the inferior olive. Nara Advanced Institute of Science and Technology Master's Thesis, 4318.

Schweighofer, N., Doya, K., Fukai, H., Chiron, J., Furukawa, T., & Kawato, M. (2004). Chaos may enhance information transmission in the inferior olive. *Proceedings of the National Academy of Sciences of the United States of America*, *101*, 4655–4660.

Schweighofer, N., Doya, K., & Kawato, M. (1999). Electrophysiological properties of inferior olive neurons: a compartmental model. *Journal of Neurophysiology*, *82*(2), 804–817.

Shinomoto, S., Miura, K., & Koyama, S. (2005). A measure of local variation of inter-spike intervals. *BioSystems*, *79*(1–3), 67–72.

Sotelo, C., Gotow, T., & Wassef, M. (1986). Localization of glutamic-acid-decarboxylase-immunoreactive axon terminals in the inferior olive of the rat, with special emphasis on anatomical relations between GABAergic synapses and dendrodendritic gap junctions. *Journal of Comparative Neurology*, *252*, 32–50.

Sotelo, C., Llinás, R., & Baker, R. (1974). Structural study of inferior olivary nucleus of the cat: morphological correlates of electrotonic coupling. *Journal of Neurophysiology*, *37*, 541–559.